magnetochemistry

MDPI

Article

Magnetically Recoverable Fe_3O_4-Cu Composite Particles with Strain-Dependent Antibacterial Activity

Nicolaza Pariona [1,2], Joaquin Garcia [1], Ecson Flores [1], Luz Esmeralda Román Mendoza [1], Noemi Raquel Checca Huaman [3], José L. Solís [1], Monica M. Gómes [1] and Marco A. Morales [1,4,*]

1 Facultad de Ciencias, Universidad Nacional de Ingeniería, Lima 15333, Peru; jsolis@uni.edu.pe (J.L.S.)
2 Red de Estudios Moleculares Avanzados, Instituto de Ecología A.C., Carretera Antigua Coatepec 351, El Haya, Veracruz, Xalapa 91073, Mexico
3 Brazilian Center for Research in Physics, Rio de Janeiro 22290-180, Brazil
4 Department of Physics, Federal University of Rio Grande do Norte, Natal 59078-970, Brazil
* Correspondence: morales@fisica.ufrn.br

Abstract

Efficient water disinfection remains a critical challenge due to the persistence of waterborne pathogens. This study reports the synthesis and characterization of magnetically recoverable Fe_3O_4-Cu composite nanoparticles designed for efficient water disinfection. The particles consist of magnetite nanoparticles functionalized with metallic copper (Cu^0) nanoparticles. The nanoparticles were synthesized via oxidative coprecipitation and characterized using x-ray diffraction, Mössbauer spectroscopy, DC magnetometry and transmission electron microscopy (TEM). Antibacterial assay was conducted against *Staphylococcus aureus* and *Escherichia coli*. Rietveld refinements confirmed lattice parameters and crystallite sizes of 8.40 Å (102 nm) for Fe_3O_4 and 3.62 Å (101 nm) for Cu. The ^{57}Fe Mössbauer spectrum for Fe_3O_4, at 300 K, exhibited two sextets with isomer shifts and hyperfine magnetic fields of 0.61 mm/s (45.3 T) and 0.34 mm/s (48.9 T), corresponding to $Fe^{2.5+}$ at octahedral sites and Fe^{3+} at tetrahedral sites, respectively. The isothermal magnetization at 300 K for Fe_3O_4 showed hysteretic behavior with saturation magnetization of 80.2 emu/g, remanence of 17.9 emu/g and coercivity of 197 Oe. Antibacterial efficacy was evaluated against *Staphylococcus aureus* (Gram-positive) and *Escherichia coli* (Gram-negative) using both the poisoned food method and batch removal assays. Results demonstrated a significant strain-dependent sensitivity; Fe_3O_4-Cu NPs inhibited *S. aureus* growth at concentrations as low as 0.1 mg/mL while *E. coli* required 0.5 mg/mL for similar effects. In batch experiments, 0.5 mg/mL of NPs achieved 100% bacterial removal for *S. aureus*, whereas 0.75 mg/mL was necessary for *E. coli*. Furthermore, the magnetic core facilitated rapid separation and reusability; the NPs maintained high efficiency against both strains in a second cycle, showing no significant loss of antibacterial activity. These findings highlight the potential of Fe_3O_4-Cu nanocomposites as high-performance, reusable biocides for targeted water treatment applications.

Keywords: composite nanoparticles; magnetite; metallic copper; magnetic separation; antibacterial activity; reusability

Check for updates

Academic Editors: Chu Dai and Chen Tian

Received: 26 August 2026
Revised: 3 October 2026
Accepted: 8 October 2026
Published: 11 October 2026

Copyright: © 2026 by the authors. Licensee MDPI, Basel, Switzerland. This article is an open access article distributed under the terms and conditions of the Creative Commons Attribution (CC BY) license.

1. Introduction

The presence of pathogenic microorganisms in water poses a severe and escalating threat to global public health and necessitates the development of advanced disinfection technologies [1]. Traditional disinfection strategies, such as chlorination, are increasingly

scrutinized due to the formation of toxic disinfection byproducts and the rapid emergence of multi-drug-resistant bacterial strains [2,3]. Consequently, there is an urgent demand for alternative, broad-spectrum antimicrobial agents that can efficiently sanitize water systems without generating secondary environmental hazards.

Among various strategies, copper-based nanomaterials have emerged as potent antimicrobial agents due to their broad-spectrum activity and multiple mechanisms of action, such as membrane disruption and oxidative stress [4–7]. Metallic copper (Cu°) has garnered significant attention as a cost-effective alternative to silver, offering high biocidal efficiency through the sustained release of ions and direct contact-killing effects [5,8–11]. However, the practical application of free-standing nanoparticles in water treatment is often hindered by the difficulty of recovering them from treated water streams. To overcome these bottlenecks, engineering functionalizing magnetite nanoparticle with a copper presents a highly promising solution. This design utilizes the copper for localized antibacterial action while leveraging the magnetic core to enable rapid, non-destructive particle recovery using an external magnetic field. Fe_3O_4 nanoparticles are highly effective, eco-friendly alternatives for water treatment due to their magnetic properties, large reactive surface area, and cost-effective recovery [12,13]. Unlike traditional water treatment chemicals that generate massive volumes of secondary sludge, magnetite nanoparticles can be easily recaptured from water streams using an external magnetic field. This makes them highly reusable and minimizes secondary waste. Compared to other externally applied stimuli utilized in advanced materials manipulation—such as electric fields, light, or thermal actuation—magnetic-field-based control offers distinct operational benefits for environmental remediation [14,15]. While light-driven or thermal responsive systems are severely attenuated in opaque, turbid, or highly contaminated aqueous media, magnetic fields enable completely contactless, non-destructive, and reversible manipulation of responsive colloidal structures [16]. Furthermore, magnetic separation operates independently of changes in the surrounding chemical environment (such as pH or ionic strength changes required by some smart polymers), making Fe_3O_4 the ideal recoverable building block for scalable water-treatment systems.

To achieve optimal core properties, oxidative coprecipitation was strategically chosen as the synthesis route in this study. Compared to other intensive thermal or chemical methodologies, this approach offers distinct advantages: it is a highly cost-effective, scalable, and environmentally friendly process that successfully yields highly crystalline and magnetically responsive magnetite cores under mild operating temperatures, avoiding the structural degradation of the core or the necessity of toxic surfactants.

Recent studies have explored composites like Cu-doped Fe_3O_4 [17], Fe_3O_4/Cu/CuO [18] magnetic nanoparticles against *E. coli* and *S. aureus*. Despite these advances, achieving a stable core–shell structure that maintains efficacy across different bacterial strains remains a subject of intense research. Gram-negative and Gram-positive bacteria exhibit distinct cell wall architectures—such as the thick peptidoglycan layer in *S. aureus* versus the lipid-rich outer membrane in *E. coli*—which significantly influence their susceptibility to metallic biocides [19]. Furthermore, the reusability of these magnetic composites is crucial for their industrial implementation, with some materials maintaining high efficiency even after multiple cycles.

In this work, we synthesized Fe_3O_4-Cu composite nanoparticles and systematically evaluated their antibacterial performance against *E. coli* and *S. aureus*. The main novelty of this study lies in the strategic synthesis of an exceptionally stable, non-oxidized metallic copper (Cu°) nanoparticles deposited over a highly magnetic core, demonstrating a highly sensitive, strain-dependent antibacterial mechanism. While previous works often require high concentrations or suffer from rapid copper oxidation, our composite nanoparticles offer tailored biocide delivery that selectively target Gram-positive over Gram-negative

pathogens, providing a high-performance, magnetically recoverable platform for selective water disinfection. Furthermore, we demonstrate that the dual-functional nanocomposite balances outstanding biocidal delivery with exceptional structural stability and magnetic responsiveness, enabling total material recovery and complete performance retention over consecutive cycles.

2. Materials and Methods

2.1. Chemicals

All the reagents used for the nanoparticle synthesis were of analytical grade and used as received without further purification. These included sodium citrate tribasic dihydrate (≥99.0%, Fermont, Monterrey, Mexico), ferrous sulfate heptahydrate (≥99.0%, Oxford, Maharashtra, India), copper (II) sulfate pentahydrate (≥99.0%, J.A. Elmer, Lima, Peru), ascorbic acid (≥99.0%, Central Drug House, Daryaganj, India), sodium hydroxide (≥97.0%, Spectrum, Gardena, California, USA), and potassium nitrate (≥99.8%, Central Drug House, New Delhi, India). All aqueous solutions were prepared using distilled water (DW).

2.2. Synthesis of Magnetite Nanoparticles (Fe_3O_4 NPs)

Magnetite nanoparticles (Fe_3O_4 NPs) were synthesized via an oxidative precipitation method [20]. Initially, 0.05 M (1.47 g) of sodium citrate tribasic dihydrate was dissolved in 95 mL of DW at 70 °C under mechanical stirring (800 rpm). Subsequently, 2 M (8 g) of NaOH and 0.5 M (5 g) of KNO_3 were added to the solution. Upon reaching homogeneity, the temperature increased to 100 °C, and 0.1 M (2.78 g) of $FeSO_4.7H_2O$ previously dissolved in 5 mL of DW was added. The reaction was maintained at 100 °C for 1 h to ensure complete NPs formation. The resulting dispersion was cooled to room temperature and washed repeatedly with DW until a neutral pH was achieved. Finally, magnetic powder was dried at 70 °C for 24 h.

2.3. Synthesis of Fe_3O_4-Cu Composite

To synthesize Fe_3O_4-Cu, Fe_3O_4 nanoparticles were used as seeds. Typically, 0.4 g of magnetite NPs were sonicated in 20 mL of H_2O for 10 min. In a separate flask, 0.005 mol of sodium citrate was dissolved in 40 mL water. The dispersion and the solution were then combined under mechanical stirring at 800 rpm. Then, 0.01 mol of $CuS0_4.5H_2O$ dissolved in 40 mL of DW was added to the mixture. After the complete dissolution of the copper salt, 0.01 mol of $C_6H_8O_6$ was added, and the temperature was raised to 80 °C. Afterwards, 1.2 g of NaOH dissolved in 30 mL of DW was added, and the temperature was increased to 100 °C. The resulting mixture was maintained under stirring for 1 h. Subsequently, the dispersion was cooled to room temperature and washed repeatedly with water until neutral pH (pH = 7) was achieved. Finally, magnetic powder was dried at 70 °C for 24 h.

2.4. Characterization of the Synthesized Nanoparticles

Several characterization techniques were applied to the synthesized materials to evaluate their structure, morphology and magnetic properties.

X-ray diffraction (XRD) measurements were performed using a Bruker D8-Advance diffractometer (Madison, Wisconsin, USA) equipped with a Cu X-ray source (λ = 1.543 Å). The diffraction patterns were collected in the 2θ range from 25° to 80° at a step size of 0.02°. Structural refinement was subsequently carried out via the Rietveld method using the MAUD version 3.07 (Materials Analysis Using Diffraction) software.

The morphology of the powders was characterized by transmission electron microscopy (TEM) using a Jeol JEM-2100 microscope (Akishima, Tokio, Japan).

^{57}Fe Mössbauer spectroscopy was employed to identify the iron phases and provide complementary structural information. The spectra were recorded at 300 K in the transmission mode using a ^{57}Co:Rh radioactive source and analyzed with Normos version 90 software. All isomer shifts are reported in relation to α-Fe.

Finally, isothermal magnetization measurements were performed at 300 K using a LakeShore, model 7400 vibrating sample magnetometer (VSM) (Westerville, OH, USA).

2.5. Antibacterial Activity Assays

The antibacterial activity of Fe_3O_4-Cu composite NPs was evaluated against *Escherichia coli* (Gram-negative) and *Staphylococcus aureus* (Gram-positive) to compare their efficacy across different bacterial types. To prepare the working inoculant, single colonies were transferred from stock plates into 10 mL of Tryptic Soy Broth (TSB) and incubated at 35 °C for 24 h. Following incubation, the cultures were centrifuged at 3500 RPM for 5 min and washed twice with a potassium phosphate buffer (0.3 mM KH_2PO_4, pH 7.2). Initial suspensions were adjusted to a cellular density of 1.5–3.0 × 10^8 CFU/mL, corresponding to optical density values at 475 nm according to ASTM E2149. These were subsequently diluted to reach a working concentration of 1.5–3.0 × 10^4 CFU/mL for both strains.

The antibacterial effect was first examined using an adapted poisoned food method. Specific masses of Fe_3O_4-Cu composite NPs were added to 15 mL of Tryptic Soy Agar (TSA) to achieve final concentrations of 0.1, 0.25, 0.5, 0.75, and 1.0 mg/mL. The mixtures were sonicated for 15 min, sterilized at 121 °C for 15 min, and poured into sterile Petri dishes. Each plate was inoculated with 100 µL of the bacterial suspension. Two controls were used: one without nanoparticles and another containing only Fe_3O_4 NPs. After incubation at 35 °C for 24 h, the survival rate was determined using the formula: CFU/mL = N × D × 10 (where N is the number of colonies and D is the dilution factor).

For the batch removal experiments, 50 mL of bacterial suspension (1.5–3.0 × 10^5 CFU/mL) was added to Erlenmeyer flasks containing Fe_3O_4-Cu NPs at concentrations of 0.5, 0.75, and 1.0 mg/mL. The mixtures were stirred at 180 rpm and 35 °C for 1 h. Subsequently, 1 mL aliquots were collected, and a magnet was used to sequester the magnetic NPs. Serial dilutions were performed, and 100 µL of the 10^{-3} and 10^{-4} dilutions were spread onto TSA medium. After incubation at 35 °C for 24 h, the colonies were counted and the CFU/mL was calculated as previously described. All experiments were performed in triplicate.

2.6. Statistical Analysis

The experiments were conducted using a completely randomized design with three independent replicates (n = 3) for each treatment. Experimental data for the bacterial inhibition percentage against *Staphylococcus aureus* and *Escherichia coli* were expressed as the mean value ± standard deviation (SD). Prior to inferential analysis, the assumptions of normality and homogeneity of variances were verified using Shapiro–Wilk and Levene's tests, respectively. Significant statistical differences among the treatments were determined through a one-way analysis of variance (ANOVA). In cases where significant effects were detected ($p < 0.05$), Tukey's Honestly Significant Difference (HSD) post hoc multiple comparison test was performed for mean separation and grouping at a significance level of $\alpha = 0.05$. All statistical analyses and bar chart visualizations were performed using the software OriginPro 2019.

3. Results and Discussion

3.1. Characterization of Magnetic NPs

3.1.1. Structural Characterization

The experimental and Rietveld-refined X-ray diffraction (XRD) patterns are displayed in Figure 1. The pure iron oxide sample showed diffraction peaks characteristic of the Fe_3O_4 phase, Figure 1A. Refinement was performed using the Crystallographic Information File (CIF) No. 1011084 from the Inorganic Crystal Structure Database (ICSD). Magnetite crystallizes in a cubic structure within the Fd-3m:1 space group. The calculated lattice parameters were a = b = c = 8.40 Å, which is in close agreement with the expected value for bulk Fe_3O_4 phase [21].

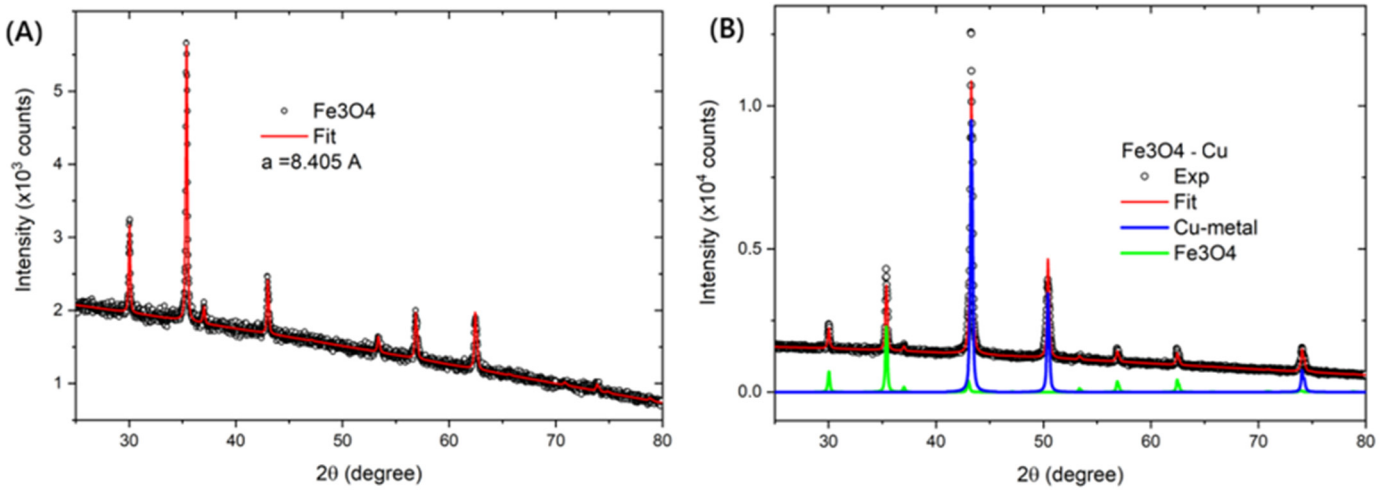


Figure 1. XRD patterns of samples (**A**) Fe_3O_4 and (**B**) Fe_3O_4-Cu composites.

The XRD pattern of the Fe_3O_4-Cu composite sample (Figure 1B) was refined using CIF No. 1011084 for Fe_3O_4 and CIF No. 7954 for metallic Cu. The Copper phase belongs to the Fm-3m space group, yielding lattice parameters of a = b = c = 3.62 Å. The structural and crystalline parameters extracted from the Rietveld refinements are summarized in Table 1.

Table 1. Structural and crystalline parameters obtained from Rietveld refinements of Fe_3O_4 and Fe_3O_4-Cu composite nanoparticles.

Sample/Phases	Lattice Parameter *a* (Å)	Phase Fraction (wt.%)	Crystallite Size *D* (nm)	Microstrain (ε)
Fe_3O_4	8.405	100	113.5	7.06×10^{-4}
Fe_3O_4-Cu:				
Fe_3O_4	8.402	18.2	102.3	4.39×10^{-6}
Cu	3.621	81.8	100.1	1.48×10^{-6}

3.1.2. Magnetic Characterization

The Mössbauer spectra displayed in Figure 2 exhibit a superposition of two magnetic sextets (S_1 and S_2), with no detectable paramagnetic components. The relative area ratio of the peaks for both sextets conform to the 3:2:1:1:2:3 line-intensity pattern, a distinctive characteristic of magnetically blocked Fe_3O_4 nanoparticles.

The sextet S_1 is assigned to the mixed-valence $Fe^{2.5+}$ state at the octahedral sites (*B*-sites). This time-averaged electronic state originates from rapid electron hopping between adjacent Fe^{2+} and Fe^{3+} cations within the inverse spinel structure, occurring on a timescale much faster than the Mössbauer characteristic measurement time. Conversely, sextet S_2 corresponds to Fe^{3+} ions located at the tetrahedral sites (*A*-sites). The ferrimagnetic nature

of magnetite arises from the antiparallel alignment of the magnetic moments between these tetrahedral and octahedral sublattices.

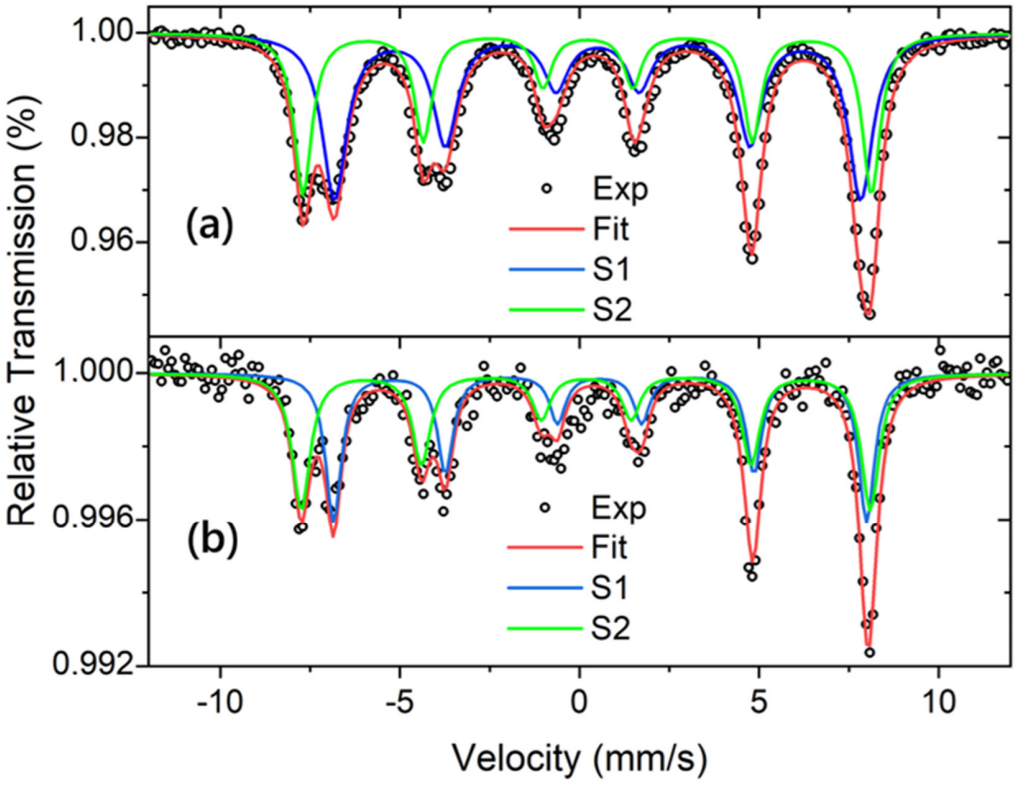


Figure 2. ^{57}Fe Mössbauer spectra recorded at 300 K for sample (**a**) Fe_3O_4 and (**b**) Fe_3O_4-Cu composite.

The obtained isomer shift (IS) and hyperfine magnetic field (Bhf) values are consistent with those expected for magnetite. Specifically, the sextet S_1 associated with the $Fe^{2.5+}$ state exhibits a higher IS and a lower Bhf value, whereas the Fe^{3+} state (S_2) displays a lower IS and a higher Bhf field value, in agreement with the literature [21]. The hyperfine parameters are summarized in Table 2.

Table 2. Hyperfine parameters extracted from the Mössbauer spectra recorded at 300 K for the Fe_3O_4 and Fe_3O_4-Cu composite nanoparticles.

	IS (mm/s)	Δ QS (mm/s)	Bhf (T)	Area (%)
Fe_3O_4:				
S_1 ($Fe^{2.5+}$)	0.61	−0.003	45.3	58
S_2 (Fe^{3+})	0.34	−0.013	48.9	42
Fe_3O_4-Cu:				
S_1 ($Fe^{2.5+}$)	0.65	−0.003	46.1	55
S_2 (Fe^{3+})	0.31	−0.013	49.1	45

Note: IS is isomer shift, Δ QS is quadrupole shift, Bhf is hyperfine magnetic field, Area is relative absorption area.

The relative absorption area of each component reflects the iron population occupying each specific crystallographic site. In this study, the integrated area ratio $A(S_1)/A(S_2)$ = 58/42 = 1.38 was used to evaluate the stoichiometry of the magnetite. Ideally, stoichiometric magnetite exhibits a theoretical area ratio of 2.0. The lower $A(S_1)/A(S_2)$ ratio obtained for our sample indicates a slight oxidation of Fe^{2+} to Fe^{3+}, leading to a non-stoichiometric magnetite structure.

The isothermal magnetizations (M vs. H) loops recorded at 300 K are shown in Figure 3. The curves exhibit a hysteretic behavior, indicating that both samples are magnetically blocked [22], which agrees with the Mössbauer study. The coercivity field (*Hc*), saturation magnetization (*Ms*) and remanent magnetization (*Mr*) for the Fe_3O_4 and Fe_3O_4-Cu samples are 197 and 177 Gauss; 80.2 and 16.1 emu/g; 17.9 and 3.1 emu/g, respectively. The *Ms* value for Fe_3O_4 sample is lower than that expected for bulk magnetite (Cullity & Graham, 2008) [22], which is attributed to a lower Fe^{3+}/Fe^{2+} ratio compared to stoichiometric magnetite. According to the XRD analysis the amount of magnetite is 18.2 wt%, thus one can calculate the Ms value of the Fe_3O_4-Cu composite considering only the Fe-oxide mass: Ms = 16.1/0.182 = 88.5 emu/g, this value is like the one for Fe_3O_4 sample. This result indicates that the addition of Cu does not affect the intrinsic magnetic response of Fe_3O_4. Finally, the Fe_3O_4-Cu composite nanoparticles possess sufficient magnetization for practical applications, such as magnetic separation from aqueous dispersions.

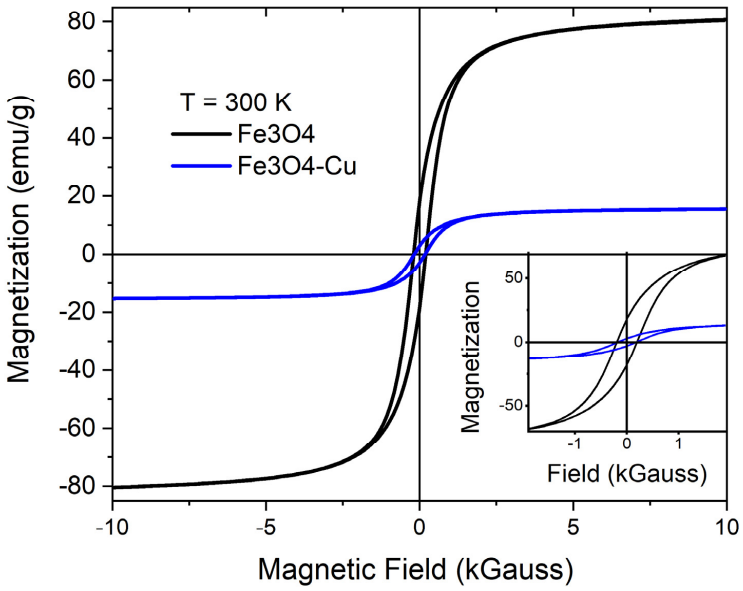


Figure 3. Isothermal magnetization recorded at 300 K for sample Fe_3O_4 and Fe_3O_4-Cu.

3.1.3. Morphological Characterization

The TEM image (Figure 4a) shows agglomerated Cu and Fe_3O_4 particles. Figure 4b shows the EDS image with colored pixels representing Cu, Fe, and O elements. The blue spots, corresponding to Fe, are uniformly distributed throughout the image. In contrast, a few large green spots, corresponding to Cu particles smaller than 1 μm, are observed. It is evident that the Cu and Fe_3O_4 phases are interconnected, as the particles were removed using a magnet during the final synthesis step.

Individual Fe, Cu and O maps are shown in Figure 4c–e. The image of Cu map shows that big Cu particles are sparsely distributed among the magnetite particles. However, dim Cu spots are visible throughout the image, suggesting that Cu has also been deposited on the surface of the magnetite particles. In a similar way, oxygen is observed in regions containing Fe_3O_4 and Cu particles, indicating the formation of a very fine oxide layer on the surface of the Cu particles. Since the XRD analysis did not detect any Cu oxide phases, the concentration of this oxide must be below the detection limit of the x-ray diffraction technique.

Therefore, the characterizations confirmed that the metallic copper (Cu°) nanoparticles are deposited onto the Fe_3O_4 core.

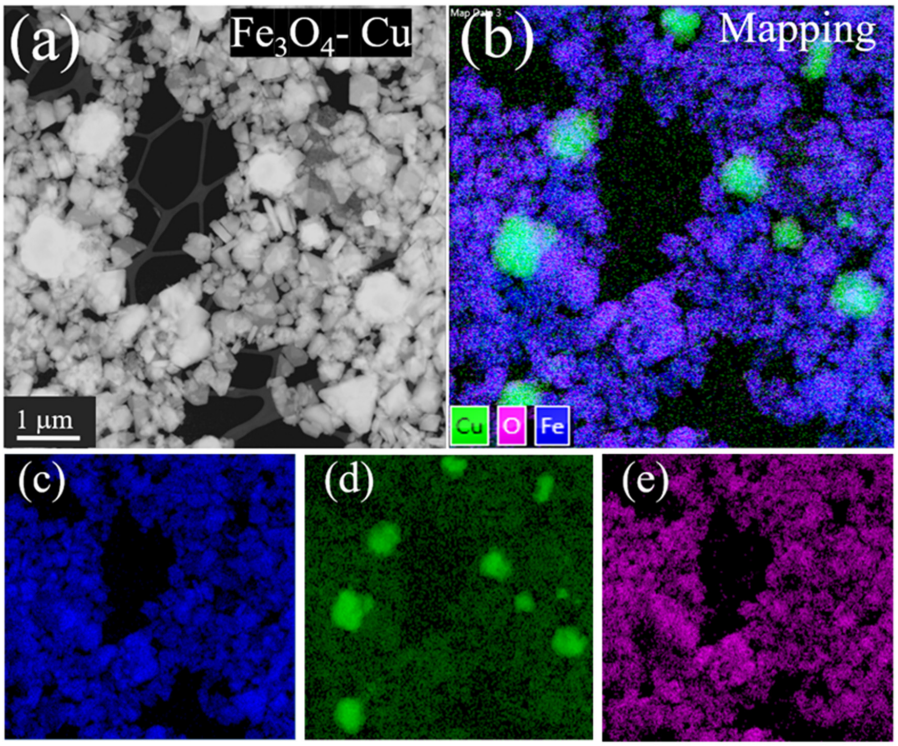


Figure 4. (**a**) TEM image of Fe_3O_4-Cu composite particles, (**b**) EDS mapping of Cu, Fe and O elements in the NPs. Individual EDS mapping for (**c**) Fe, (**d**) Cu and (**e**) O.

Figure 5a shows an isolated composite particle and Figure 5b–e shows the EDS map for Fe, Cu, and O elements. Figure 5a shows that the metal Cu particles and the Fe-oxide particles form a solid composite. Figure 5f shows the same particle in which a straight line is drawn for the EDS scan. Figure 5g shows the Cu, Fe and O Kα1 signals detected along the 400 nm line. The EDS intensities from the Fe and O elements are similar and are due to the Fe_3O_4, whereas the Cu signal is nine-fold greater than the Fe and O signals, suggesting that Cu is mostly in the metallic state; however, we cannot rule out the presence of a fine layer of CuO.

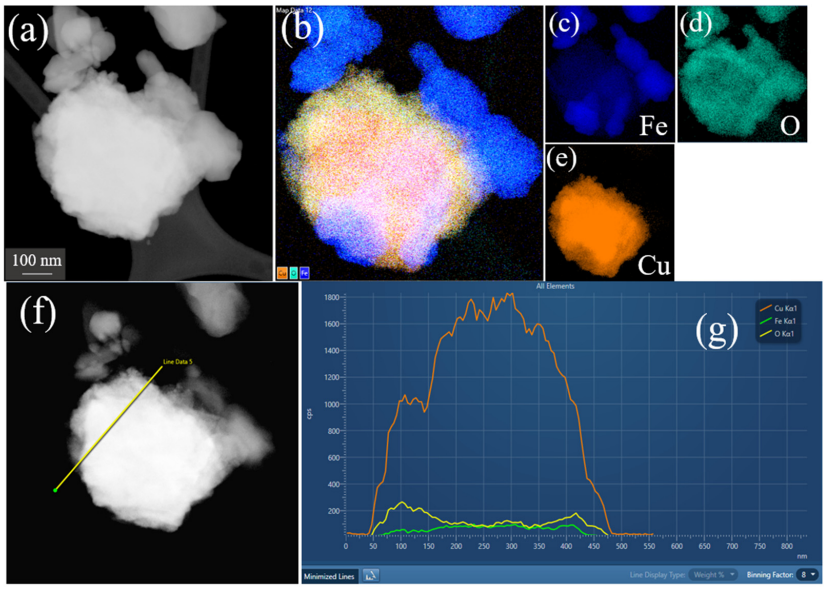


Figure 5. (**a**) TEM image of Fe_3O_4-Cu composite particle, (**b**) EDS global mapping of Cu, Fe and O elements in the composite NP. Individual EDS mapping for (**c**) Fe, (**d**) O and (**e**) Cu. (**f**) Line for EDS scanning. (**g**) Kα1 scans for Cu (orange line), Fe (green) and O (yellow).

3.2. Antibacterial Efficacy via Poisoned Food Method

Macroscopic inspection of the agar plates via the poisoned medium assay (Figure 6) visually confirmed the differential susceptibility profiles and qualitative trends of the samples. In the row corresponding to *Staphylococcus aureus* (Figure 6a), a dense and uniform bacterial lawn was observed on both the control plate and the plate treated with Fe_3O_4 alone (0.5 mg/mL), ratifying the low intrinsic antimicrobial activity of the pure magnetite core matrix. However, total macroscopic eradication (absolute absence of visible colonies) was evidenced in all plates containing the Fe_3O_4-Cu composite NPs, ranging from the lowest dose of 0.1 mg/mL up to the concentration of 1.0 mg/mL, demonstrating the rapid bactericidal action of copper against this Gram-positive strain. On the other hand, the row corresponding to *Escherichia coli* (Figure 6b) visually exhibited a clear dose-dependent response. While the control and Fe_3O_4 alone (0.5 mg/mL) plates maintained massive bacterial proliferation, the plates treated with Fe_3O_4-Cu NPs showed a progressive and gradual reduction in the density of colony-forming units (CFUs) as the concentration increased from 0.1 to 0.5 mg/mL. Finally, a complete visual inhibition and total absence of microbial growth were verified in the plates corresponding to the 0.75 and 1.0 mg/mL concentrations, showcasing the critical saturation threshold and the higher biological resistance presented by this Gram-negative bacterium against sub-lethal concentrations of the bimetallic material.

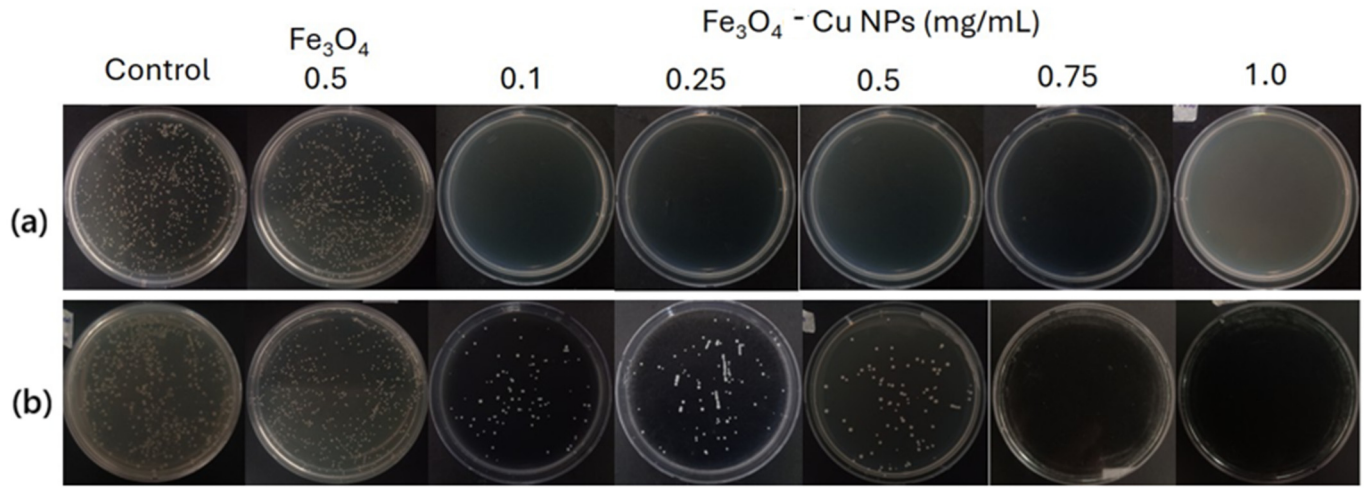


Figure 6. Macroscopic antibacterial activity of Fe_3O_4-Cu composite NPs using the poisoned medium assay against (**a**) *Staphylococcus aureus* and (**b**) *Escherichia coli.* Representative agar plates are displayed for the control (Blank), the Fe_3O_4 matrix (0.5 mg/mL), and various concentrations of the bimetallic composite (0.1, 0.25, 0.5, 0.75, and 1.0 mg/mL) after 24 h of incubation.

The one-way analysis of variance (ANOVA) numerically supported these macroscopic observations, revealing highly significant statistical differences among the evaluated treatments for both *S. aureus* ($p < 0.001$) and *E. coli* ($p < 0.001$). According to the quantitative data in Table 3, for *S. aureus* the control group (without NPs) showed no inhibition (0.00%) whereas the Fe_3O_4 core alone exhibited partial inhibitory activity of 21.13%. Remarkably, the incorporation of copper onto the magnetite surface drastically enhanced the bactericidal effect, achieving a perfect 100% inhibition from the lowest concentration (0.1 mg/mL). Tukey's HSD test confirmed that all Fe_3O_4-Cu NPs concentrations (0.1 to 1.0 mg/mL) grouped within the same statistical category (letter c, $p > 0.05$), demonstrating that the minimum dose is sufficient to achieve complete eradication.

Table 3. Antibacterial activity via the poisoned medium assay of Fe_3O_4 NPs and the Fe_3O_4-Cu composite NPs at different concentrations against *Staphylococcus aureus* and *Escherichia coli*.

Nanoparticles	Concentration (mg/mL)	*S. aureus* (%) ± DS	*E. coli* (%) ± DS
Control	0.0	0.0 ± 0.0 a	0.0 ± 0.0 a
Fe_3O_4	0.5	21.1 ± 4.3 b	1.57 ± 1.1 a
Fe_3O_4-Cu	0.1	100 ± 0.0 c	55.5 ± 1.1 b
	0.25	100 ± 0.0 c	63.3 ± 0.8 c
	0.5	100 ± 0.0 c	68.3 ± 0.8 d
	0.75	100 ± 0.0 c	99.3 ± 0.3 e
	1.0	100 ± 0.0 c	99.6 ± 0.2 e

Note: Values are expressed as mean ± standard deviation of three independent replicates (n = 3). Different lowercase letters within the same column indicate highly significant statistical differences among treatments according to Tukey's Honestly Significant Difference (HSD) post hoc test ($p < 0.05$).

Conversely, the quantification inhibition against *E. coli* (Table 3) displayed distinct, gradual dose-dependent behavior. Treatment with Fe_3O_4 NPs alone showed no real antimicrobial effect (1.56%), sharing the same statistical significance as the control ($p > 0.05$). However, upon applying the Fe_3O_4-Cu composite NPs, the inhibition percentage increased significantly with each concentration step: 55.54% for 0.1 mg/mL, 63.32% for 0.25 mg/mL, and 68.34% for 0.5 mg/mL. Maximum efficacy was reached at 0.75 mg/mL (99.31%) and remained statistically unchanged when increasing the dose to 1.0 mg/mL (99.65%), as no significant differences were observed between both treatments ($p > 0.05$).

When comparing the antibacterial performance of the synthesized Fe_3O_4-Cu composite NPs with the recent literature, our material demonstrates superior or competitive efficacy at significantly lower concentrations and shorter incubation times. For instance, some studies reported that the bare Fe_3O_4 exhibited moderate antibacterial activity against *E. coli* and *S. aureus* [17,23]. This aligns with our findings for the pure magnetite core (Fe_3O_4 at 0.5 mg/mL), which achieved only 21.1% and 1.57% inhibition, respectively, confirming that Fe_3O_4 alone possess limited intrinsic bactericidal traits. However, the antibacterial activity can be increased through surface modification of Fe_3O_4. Recently, Zhang et al. reported a 94.8% inhibition of *E. coli* using 1.0 mg/mL of Cu^{2+}-Fe_3O_4 nanocomposites [17]. Also, Sharaf et al. reported that rhamnolipid-coated iron oxide nanoparticles showed notable antibacterial efficacy against several *E. coli* and *S. aureus* [24]. In comparison, our Fe_3O_4-Cu composite NPs architecture optimized this threshold, reaching a massive 99.31% inhibition against *E. coli* at a much lower dose of 0.75 mg/mL and complete eradication (100%) at 1.0 mg/mL. Meanwhile, a 100% inhibition against *S. aureus* was achieved from the lowest concentration evaluated (0.1 mg/mL). This enhanced performance is attributed to the high surface-area-to-volume ratio of the copper particles assembled over the magnetic core, which promotes a more rapid and concentrated release of bactericidal Cu^{2+} ions directly onto the negatively charged bacterial membranes.

3.3. Antibacterial Activity in Aqueous Suspension and Reuse Assays

The Fe_3O_4 core serves not only as support but also as a functional handle for reusability. The ability to separate the NPs using an external magnet is a significant advantage for water treatment or batch sterilization, as it prevents secondary contamination by the nanomaterials themselves. Complementary aqueous suspension assays and their respective reuse (recyclability) cycles confirmed the high efficiency and robustness of the structured Fe_3O_4-Cu composite NPs ($p < 0.001$). The compiled data in Table 4 demonstrated that for *S. aureus*, all tested concentrations (0.5, 0.75, and 1.0 mg/mL) maintained massive and stable inhibition levels (ranging from 99.7 to 100%), clustering uniformly under the

same statistical category ($p > 0.05$) relative to the control. Crucially, no loss of bactericidal activity was detected between the first-use cycle (1st) and the reuse cycle (2nd), ratifying the structural stability of the material under the tested conditions. Nevertheless, it is important to note that full physical characterization of the post-use nanoparticles (e.g., spent XRD or leaching analysis) was limited by the small sample mass recovered at these benchmarking concentrations. Future scaling experiments will focus on quantifying chemical leaching thresholds and structural evolution over extended operation.

Table 4. Evaluation of the reusability and stability of Fe_3O_4-Cu NPs in aqueous suspension against *Staphylococcus aureus* and *Escherichia coli*.

Concentration (mg/mL)	Reuse Cycle	*S. aureus* (%)	*E. coli* (%)
0.0	1st	0.0 ± 0.0 a	0.0 ± 0.0 a
0.0	2nd	0.0 ± 0.0 a	0.0 ± 0.0 a
0.5	1st	99.7 ± 0.4 b	9.1 ± 2.1 b
0.5	2nd	99.7 ± 0.3 b	10.1 ± 0.8 b
0.75	1st	100 ± 0.0 b	99.5 ± 0.4 c
0.75	2nd	100 ± 0.0 b	99.3 ± 0.3 c
1.0	1st	100 ± 0.0 b	100 ± 0.0 c
1.0	2nd	100 ± 0.0 b	100 ± 0.0 c

Note: Values are expressed as the mean percentage of inhibition ± standard deviation of three independent replicates ($n = 3$). Different lowercase letters within the same column denote highly significant statistical differences among treatments and their respective recyclability cycles according to Tukey's Honestly Significant Difference (HSD) post hoc test ($p < 0.05$). Treatments labeled as "Reuse" correspond to the second consecutive biological disinfection cycle using the recovered material.

For *E. coli*, the aqueous suspension (Table 4), the strong dose-dependent nature of the Fe_3O_4-Cu NPs was reconfirmed. The low concentration (0.5 mg/mL) was inefficient to control the Gram-negative pathogen, achieving only 9.14% inhibition in the first cycle and 10.1% upon reuse. However, increasing the dose to 0.75 mg/mL caused the bactericidal activity to elevate exponentially to 99.5% (1st) and 99.3 (2nd). When evaluating the maximum dose of 1.0 mg/mL, absolute elimination (100.0%) was achieved in both cycles. Notably, for both bacteria, no significant statistical differences were detected between the fresh (first-use) samples and their corresponding reuses ($p > 0.05$), rigorously demonstrating the excellent structural stability and reusability of the Fe_3O_4-Cu NPs in aqueous media.

The reusability profiles established in our study surpass those of typical non-magnetic metallic nanocomposites. Previous reports 10% Cu^{2+}-Fe_3O_4 nanoparticles note a drop in efficacy during consecutive reuse cycles against *E. coli* [17]. Conversely, the Fe_3O_4-Cu NPs framework maintained near-perfect antibacterial stability (>99%) during reuse assays for both strains. The magnetic core not only prevents severe nanoparticle sintering but also enables instantaneous and total material recovery via an external magnetic field, minimizing mass loss and demonstrating a highly sustainable and cost-effective approach for real-world environmental and water disinfection applications. Although magnetic separation temporarily concentrates the nanoparticles, the soft magnetic properties of the magnetite core allow the composite structure to easily redisperse upon mechanical agitation or mild sonication once the external magnetic field is removed, preventing irreversible agglomeration. While this dual-cycle evaluation serves as a successful proof-of-concept for the short-term stability of the Cu^0 particles, further long-term cycling assays (e.g., 5 to 10 cycles) will be valuable in future studies to determine the maximum operational lifespan and the exact cumulative aggregation limits of the composite.

The Fe_3O_4-Cu composite NPs exhibited a clear dose-dependent inhibitory effect against both tested strains, with *S. aureus* showing significantly higher susceptibility than *E. coli*. For the Gram-positive *S. aureus*, growth inhibition was observed at a minimum concentration of 0.1 mg/mL. In contrast, the Gram-negative *E. coli* required five-fold higher concentration, with effective inhibition starting at 0.5 mg/mL. While bare Fe_3O_4 nanoparticles exhibit a minor background inhibitory baseline (~21.1% as shown in Table 3), they lack the capacity for total bacterial eradication. In contrast, the functionalization with the metallic cooper nanoparticles introduces a massive synergistic effect, drastically amplifying the biocide delivery. Control groups (NP-free agar) showed no inhibitory activity, confirming that the antibacterial properties are derived from copper functionalization.

3.4. Antibacterial Mechanism

The marked difference in the biological susceptibility profiles between *S. aureus* and *E. coli*, is directly attributed to the structural discrepancies in their cell wall compositions. The cell wall of the Gram-positive bacterium *S. aureus* consists of a thick but porous peptidoglycan layer that lacks a protective outer membrane. This molecular framework acts as a negatively charged sieve due to the abundance of teichoic acids [25], which promotes a strong electrostatic attraction with the copper ions (Cu^{2+}) continuously released from the surface of the Fe_3O_4-Cu composite NPs. This massive electrostatic affinity facilitates the immediate accumulation of metal ions on the cellular surface, triggering cell wall lysis and subsequent material penetration, which explains why 100% inhibition is achieved from the minimum concentration (0.1 mg/mL). Conversely, the Gram-negative bacterium *E. coli*, possesses a more complex cellular structure characterized by an outer lipopolysaccharide (LPS) membrane covering a thin peptidoglycan layer [25]. This outer membrane functions as a highly selective hydrophobic barrier that restricts the passive diffusion of macromolecules and exogenous metallic cations [26]. At sub-lethal concentration (0.1 to 0.5 mg/mL) the LPS membrane partially absorbs and neutralizes the initial ions flux, thereby mitigating the immediate bactericidal damage ang generating the gradual, dose-dependent response observed visually. However, upon reaching the critical threshold of 0.75 mg/mL, the saturation of copper ions overwhelms the lipopolysaccharide binding sites, displacing essential magnesium and calcium ions that stabilize the membrane [27,28]. This triggers a phenomenon known as "self-promoted uptake", disrupting the outer membrane permeability and allowing massive influx of copper into the cytoplasm [29]. Beyond the distinct envelope architectures of the targeted pathogens, the biological response is deeply governed by the fundamental nano–bio interaction principles, where nanomaterial characteristics such as size and localized surface chemistry play a synergistic role. In our system, the nanoscale dimensions maximize the effective contact surface area with the lipid bilayers, while the dense the metallic Cu° particles ensures a highly localized and concentrated ion flux at the nano–bio interface. These physical parameters dictate how effectively the material overcomes the cell barrier, explaining the pronounced species-dependent threshold observed between the porous peptidoglycan matrix and the highly selective lipopolysaccharide outer membrane.

Once inside the cell (for both strains), copper ions induce multi-target synergistic toxicity. First, they catalyze Fenton-like reactions that generate an exponential spike in reactive oxygen species (ROS), such as hydroxyl radicals (OH°) [17]. These ROS cause severe lipid peroxidation in the plasma membrane, destroying the bacterial chemiosmotic potential. Second, Cu^{2+} ions exhibit a high affinity for sulfhydryl (-SH) and imidazole groups of cytoplasmic proteins, causing enzymatic denaturation and the collapse of respiratory metabolic pathways. Finally, the direct interaction of copper with the nitrogenous bases of the bacterial DNA disrupts the double-helix structure, inhibiting replication and transcrip-

tion processes (Cervantes-Cervantes et al., 2005), thereby ensuring the total eradication macroscopically observed at optimal doses.

4. Conclusions

In this study, Fe_3O_4-Cu composite nanoparticles were successfully synthesized and evaluated for both their physicochemical properties and antibacterial performance. Rietveld refinement and Mössbauer spectroscopy confirmed the high structural crystallinity of the magnetite core and the successful deposition of a metallic copper nanoparticles. Magnetic characterization of pure magnetite demonstrated robust hysteretic behavior with a high saturation magnetization of 80.2 emu/g, enabling rapid and complete separation via external magnetic fields. Regarding biological performance, the nanoparticles were successfully evaluated for their antibacterial performance, demonstrating a higher susceptibility in Gram-positive *S. aureus* compared to Gram-negative *E. coli*. The metallic copper nanoparticles (Cu°) proved to be highly effective, achieving 100% bacterial removal at concentrations as low as 0.5 mg/mL for *S. aureus* in batch systems.

A significant advantage of this composite is its magnetic functionality, which allows for rapid recovery using an external magnetic field. The reusability assays revealed that the NPs maintain excellent stability and total efficacy against both strains after consecutive cycles, with no significant loss in antibacterial activity. These results suggest that Fe_3O_4-Cu composite NPs are promising candidates for water disinfection and antimicrobial applications, offering a balance between high biocidal efficiency and the potential for material recovery, minimizing environmental release.

Author Contributions: Conceptualization, N.P., M.A.M. and J.L.S.; methodology, N.P., M.A.M., L.E.R.M. and J.L.S.; software, N.P., M.A.M. and J.L.S.; validation, N.P. and M.A.M.; formal analysis, N.P., M.A.M. and N.R.C.H.; investigation, N.P., J.G., E.F. and L.E.R.M.; resources, J.L.S. and M.M.G.; data curation, N.P., L.E.R.M. and M.A.M.; writing—original draft preparation, N.P., M.A.M., M.M.G. and J.L.S.; writing—review and editing, N.P., M.A.M. and J.L.S.; visualization, J.G., N.R.C.H. and E.F.; supervision, N.P., M.A.M. and J.L.S.; project administration, J.L.S. and M.M.G.; funding acquisition, J.L.S. and M.M.G. All authors have read and agreed to the published version of the manuscript.

Funding: This research received no external funding.

Data Availability Statement: The original contributions presented in this study are included in the article. Further inquiries can be directed to the corresponding author.

Acknowledgments: M. Morales thanks to CNPQ -305725/2024-6 and Prociencia PE501084296-2023-PROCIENCIA-BM for their fellowships.

Conflicts of Interest: The authors declare no conflict of interest.

References

1. Elhenawy, S.; Khraisheh, M.; AlMomani, F.; Al-Ghouti, M.; Selvaraj, R.; Al-Muhtaseb, A. Emerging Nanomaterials for Drinking Water Purification: A New Era of Water Treatment Technology. *Nanomaterials* **2024**, *14*, 1707. [CrossRef] [PubMed]
2. Justyna, Ł.; Magdalena, W.; Bartosz, K.; Maria, T.; Julia, K. Disinfectant-induced bacterial resistance and antibiotic cross-resistance—mechanisms and clinical relevance. *Clin. Exp. Med.* **2026**, *26*, 26. [CrossRef] [PubMed]
3. Zhao, W.; Hou, Y.; Wei, L.; Wei, W.; Zhang, K.; Duan, H.; Ni, B.J. Chlorination-induced spread of antibiotic resistance genes in drinking water systems. *Water Res.* **2025**, *274*, 123092. [CrossRef] [PubMed]
4. Ananth, A.; Dharaneedharan, S.; Heo, M.S.; Mok, Y.S. Copper oxide nanomaterials: Synthesis, characterization and structure-specific antibacterial performance. *Chem. Eng. J.* **2015**, *262*, 179–188. [CrossRef]
5. Lopez-Lima, D.; Mtz-Enriquez, A.I.; Carrión, G.; Basurto-Cereceda, S.; Pariona, N. The bifunctional role of copper nanoparticles in tomato: Effective treatment for Fusarium wilt and plant growth promoter. *Sci. Hortic.* **2021**, *277*, 109810. [CrossRef]
6. Mondaca, F.; Mtz-Enriquez, A.; Pariona, N. Copper-based nanostructures for plant disease management. In *Copper Nanostructures: Next-Generation of Agrochemicals for Sustainable Agroecosystems*; Abd-Elsalam, K.A., Ed.; Elsevier: Amsterdam, The Netherlands, 2022; pp. 185–201.

7. Pariona, N.; Mtz-Enriquez, A.I.; Sánchez-Rangel, D.; Carrión, G.; Paraguay-Delgado, F.; Rosas-Saito, G. Green-synthesized copper nanoparticles as a potential antifungal against plant pathogens. *RSC Adv.* **2019**, *9*, 18835–18843. [CrossRef] [PubMed]
8. Chatterjee, A.K.; Chakraborty, R.; Basu, T. Mechanism of antibacterial activity of copper nanoparticles. *Nanotechnology* **2014**, *25*, 135101. [CrossRef] [PubMed]
9. Grass, G.; Rensing, C.; Solioz, M. Metallic copper as an antimicrobial surface. *Appl. Environ. Microbiol.* **2011**, *77*, 1541–1547. [CrossRef] [PubMed]
10. Ibarra-Laclette, E.; Blaz, J.; Pérez-Torres, C.A.; Villafán, E.; Lamelas, A.; Rosas-Saito, G.; Ibarra-Juárez, L.A.; García-ávila, C.d.J.; Martínez-Enriquez, A.I.; Pariona, N. Antifungal Effect of Copper Nanoparticles against *Fusarium kuroshium*, an Obligate Symbiont of Euwallacea kuroshio Ambrosia Beetle. *J. Fungi* **2022**, *8*, 347. [CrossRef] [PubMed]
11. Pellosi, D.S.; Paiva, G.S.M.; Vital, V.G.; Mendes, A.L.; Santos, N.G.; Kuriki, F.K.; Lira, K.D.L.; Oliveira, G.C.M.; Gomes, Y.R.; Lobo, F.G.; et al. Harnessing Copper Nanoparticles for Antimicrobial Applications: Advances and Challenges. *Antibiotics* **2025**, *14*, 1170. [CrossRef] [PubMed]
12. Aly, S.T.; Saed, A.; Mahmoud, A.; Badr, M.; Garas, S.S.; Yahya, S.; Hamad, K.H. Preparation of magnetite nanoparticles and their application in the removal of methylene blue dye from wastewater. *Sci. Rep.* **2024**, *14*, 20100. [CrossRef] [PubMed]
13. Tzirini, M.; Kaprara, E.; Asimakidou, T.; Kontogiannopoulos, K.; Tzamos, E.; Kellartzis, I.; Samaras, T.; Balcells, L.; Mitrakas, M.; Simeonidis, K. Magnetically recoverable nanoparticles for the simultaneous removal of Sb and As from water. *Environ. Adv.* **2020**, *2*, 100013. [CrossRef]
14. Kim, Y.; Zhao, X. Magnetic Soft Materials and Robots. *Chem. Rev.* **2022**, *122*, 5317–5364. [CrossRef] [PubMed]
15. Yang, Z.; Zhang, L. Magnetic Actuation Systems for Miniature Robots: A Review. *Adv. Intell. Syst.* **2020**, *2*, 2000082. [CrossRef]
16. Basu, A.; Okello, L.B.; Castellanos, N.; Roh, S.; Velev, O.D. Assembly and manipulation of responsive and flexible colloidal structures by magnetic and capillary interactions. *Soft Matter* **2023**, *19*, 2466–2485. [CrossRef] [PubMed]
17. Zhang, J.; Nan, R.; Dong, Y.; Yao, J.; Liang, T.; Li, R.; Li, J.; Ferrari, P.F.; Perego, P.; Liu, B. Synthesis of Cu-Doped Fe_3O_4 Nanocomposites for Bacterial Disinfection. *J. Nanotechnol.* **2025**, *2025*, 10. [CrossRef]
18. Liu, Z.; Guo, S.; Fang, X.; Shao, X.; Zhao, Z. Antibacterial and plant growth-promoting properties of novel Fe_3O_4/Cu/CuO magnetic nanoparticles. *RSC Adv.* **2022**, *12*, 19856–19867. [CrossRef] [PubMed]
19. Metryka, O.; Wasilkowski, D.; Mrozik, A. Insight into the antibacterial activity of selected metal nanoparticles and alterations within the antioxidant defence system in *Escherichia coli*, *Bacillus cereus* and *Staphylococcus epidermidis*. *Int. J. Mol. Sci.* **2021**, *22*, 11811. [CrossRef]
20. Pariona, N.; Martínez, A.I.; Hernandez-Flores, H.; Clark-Tapia, R. Effect of magnetite nanoparticles on the germination and early growth of Quercus Macdougallii. *Sci. Total Environ.* **2017**, *575*, 869–875. [CrossRef] [PubMed]
21. Cornell, R.M.; Schwertmann, U. *The Iron Oxides: Structure, Properties, Reactions, Occurrences and Uses*; Wiley: Weinheim, Germany, 2003.
22. Cullity, B.D.; Graham, C.D. *Introduction to Magnetic Materials*, 1st ed.; Wiley: Weinheim, Germany, 2008. [CrossRef]
23. Arokiyaraj, S.; Saravanan, M.; Udaya Prakash, N.K.; Valan Arasu, M.; Vijayakumar, B.; Vincent, S. Enhanced antibacterial activity of iron oxide magnetic nanoparticles treated with *Argemone mexicana* L. leaf extract: An in vitro study. *Mater. Res. Bull.* **2013**, *48*, 3323–3327. [CrossRef]
24. Sharaf, M.; Sewid, A.H.; Hamouda, H.I.; Elharrid, M.G.; El-Demerdash, S.A.; Alharthi, A.; Hashim, N.; Hamad, A.A.; Selim, S.; M. Alkhalifah, D.H.; et al. Rhamnolipid-coated iron oxide nanoparticles as a novel multitarget candidate against major foodborne *E. coli* serotypes and Methicillin-resistant *S. aureus*. *Microbiol. Spectr.* **2022**, *10*, 1–17. [CrossRef] [PubMed]
25. Slavin, Y.N.; Asnis, J.; Häfeli, U.O.; Bach, H. Metal nanoparticles: Understanding the mechanisms behind antibacterial activity. *J. Nanobiotechnol.* **2017**, *15*, 65. [CrossRef] [PubMed]
26. Franco, D.; Calabrese, G.; Guglielmino, S.P.P.; Conoci, S. Metal-Based Nanoparticles: Antibacterial Mechanisms and Biomedical Application. *Microorganisms* **2022**, *10*, 1778. [CrossRef] [PubMed]
27. Hancock, R.E.W.; Farmer, S.W.; Li, Z.; Poolet, K. Interaction of Aminoglycosides with the Outer Membranes and Purified Lipopolysaccharide and OmpF Porin of *Escherichia coli*. *Antimicrob. Agents Chemother.* **1991**, *35*, 1309–1314. [CrossRef] [PubMed]
28. Nikaido, H. Molecular Basis of Bacterial Outer Membrane Permeability Revisited. *Microbiol. Mol. Biol. Rev.* **2003**, *67*, 593–656. [CrossRef] [PubMed]
29. Minnock, A.; Vernon, D.I.; Schofield, J.; Griffiths, J.; Parish, J.H.; Brown, S.B. Mechanism of uptake of a cationic water-soluble pyridinium zinc phthalocyanine across the outer membrane of *Escherichia coli*. *Antimicrob. Agents Chemother.* **2000**, *44*, 522–527. [CrossRef] [PubMed]

Disclaimer/Publisher's Note: The statements, opinions and data contained in all publications are solely those of the individual author(s) and contributor(s) and not of MDPI and/or the editor(s). MDPI and/or the editor(s) disclaim responsibility for any injury to people or property resulting from any ideas, methods, instructions or products referred to in the content.